

EDEN: Sensitivity Analysis and Transiting Planet Detection Limits for Nearby Late Red Dwarfs

AIDAN GIBBS,^{1,2} ALEX BIXEL,^{1,3} BENJAMIN V. RACKHAM,⁴ DÁNIEL APAI,^{1,3,5} MARTIN SCHLECKER,⁶ NÉSTOR ESPINOZA,⁷ LUIGI MANCINI,^{8,6,9,10} WEN-PING CHEN,¹¹ THOMAS HENNING,⁶ PAUL GABOR,¹² RICHARD BOYLE,¹² JOSE PEREZ CHAVEZ,¹ ALLIE MOUSSEAU,¹ JEREMY DIETRICH,¹ QUENTIN JAY SOCIA,¹ WING IP,¹¹ CHOW-CHOONG NGEOW,¹¹ ANLI TSAI,¹¹ ASMITA BHANDARE,⁶ VICTOR MARIAN,⁶ HANS BAEHR,⁶ SAMANTHA BROWN,⁶ MAXIMILIAN HÄBERLE,⁶ MIRIAM KEPPLER,⁶ KARAN MOLAVERDIKHANI,⁶ PAULA SARKIS,⁶

¹Steward Observatory, The University of Arizona, 933 N. Cherry Avenue, Tucson, AZ 85721, USA

²Department of Physics & Astronomy, University of California, Los Angeles, Los Angeles, CA 90095, USA

³NASA Nexus For Exoplanetary System Science: Earths in Other Solar Systems Team

⁴Department of Earth, Atmospheric, and Planetary Sciences and Kavli Institute for Astrophysics and Space Research, Massachusetts Institute of Technology, 77 Massachusetts Ave., Cambridge, MA 02139, USA*

⁵Lunar and Planetary Laboratory, The University of Arizona, 1640 E. University Boulevard, Tucson, AZ 85718, USA

⁶Max Planck Institute for Astronomy, Königstuhl 17, D-69117 Heidelberg, Germany

⁷Space Telescope Science Institute, 3700 San Martin Drive, Baltimore, MD 21218, USA†

⁸Department of Physics, University of Rome Tor Vergata, Via della Ricerca Scientifica 1, I-00133 Rome, Italy

⁹INAF Osservatorio Astrofisico di Torino, via Osservatorio 20, I-10025 Pino Torinese, Italy

¹⁰International Institute for Advanced Scientific Studies (IIASS), Via G. Pellegrino 19, I-84019 Vietri sul Mare (SA), Italy

¹¹Graduate Institute of Astronomy, National Central University, 300 Jhongda Road, Zhongli, Taoyuan 32001, Taiwan

¹²Vatican Observatory Research Group, University of Arizona, 933 N Cherry Ave., Tucson AZ, 85721-0065, USA

(Accepted February 20, 2020)

Submitted to AJ

ABSTRACT

Small planets are common around late-M dwarfs and can be detected through highly precise photometry by the transit method. Planets orbiting nearby stars are particularly important as they are often the best-suited for future follow-up studies. We present observations of three nearby M-dwarfs referred to as EIC-1, EIC-2, and EIC-3, and use them to search for transits and set limits on the presence of planets. On most nights our observations are sensitive to Earth-sized transiting planets, and photometric precision is similar to or better than *TESS* for faint late-M dwarfs of the same magnitude ($I \approx 15$ mag). We present our photometry and transit search pipeline, which utilizes simple median detrending in combination with transit least squares based transit detection (Hippke & Heller 2019). For these targets, and transiting planets between one and two Earth radii, we achieve an average transit detection probability of $\sim 60\%$ between periods of 0.5 and 2 days, $\sim 30\%$ between 2 and 5 days, and $\sim 10\%$ between 5 and 10 days. These sensitivities are conservative compared to visual searches.

Keywords: Exoplanets, Habitable planets, Transit photometry

1. INTRODUCTION

Planetary systems around nearby stars are set to play a particularly important role in the future of exoplanet characterization studies, yet only a very small fraction of these planets have been identified to date. Reconnaissance spectroscopy of nearby, small (Earth-sized) transiting planets is possible now with the *Hubble Space*

Telescope (e.g., as in the TRAPPIST-1 system, see de Wit et al. 2016, 2018; Zhang et al. 2018; Wakeford et al. 2019) and in-depth spectroscopic studies of these systems will be possible in the near-future with the *James Webb Space Telescope* (e.g., Greene et al. 2016; Morley et al. 2017; Lustig-Yaeger et al. 2019) and with the *ARIEL* mission (e.g., Tinetti et al. 2018). Transiting, habitable-zone, Earth-sized planets around nearby stars are likely to be the only type of habitable planets that can be characterized in detail in the next two decades.

* 51 Pegasi b Postdoctoral Fellow

† IAU-Gruber Fellow

Although only a fraction of planets happen to transit as observed from Earth, fortunately, the high frequency of M-dwarfs in the solar neighborhood, the most favorable host stars for detecting Earth-sized planets, improves the chances of a positive detection. Based on results from the RECONS group (Henry et al. 2018), there are 283 currently known M-type stars within 10 pc, and that number continues to grow. In addition, small ($1-4 R_{\oplus}$) planets are found to be very common around M-dwarfs (Dressing & Charbonneau 2015; Mulders et al. 2015a,b; Hardegree-Ullman et al. 2019). However, M-dwarfs in the solar neighborhood are located isotropically in the sky, requiring targeted, star-by-star monitoring (e.g., Nutzman & Charbonneau 2008; Jehin et al. 2011; Delrez et al. 2018). Worldwide networks of ground-based telescopes that can obtain continuous targeted coverage are therefore well-suited to search for these planets (Blake et al. 2008).

The Exoearth Discovery & Exploration Network (EDEN, PIs: D. Apai, P. Gabor, Th. Henning, W-P. Chen) is a multi-continental research network that searches for habitable-zone planets within fifty lightyears¹. EDEN’s transit survey component began in Spring 2018 and currently uses eight telescopes to search for transiting planets around nearby late M-dwarf stars, which are the easiest stars to find Earth-sized planets around. EDEN differs from other ongoing surveys in that it uses several large preexisting telescopes (>1 -m diameter) and that its longitudinally distributed stations are capable of providing continuous coverage. When no planet is found in a system, EDEN also aims to place stringent upper limits on the probability that short-period planets are present. The interpretation of such non-detections requires a robust and consistent observing strategy, thorough understanding and modeling of systematics, efficient photometric pipeline and trend removal (detrending), and a well-characterized planet-detection algorithm. With this photometric and detection pipeline, EDEN also provides an excellent telescope network for photometric follow-up of planet candidates identified by NASA’s *TESS* (Ricker et al. 2015) transit search mission.

We review here these components of our sensitivity analysis, and present example results for the first three EDEN targets searched in depth. We do not detect any convincing transit candidates for follow-up, but show that there is a high probability we would have detected Earth-sized planets with periods less than 5 days if their orbital planes were aligned with our line of sight. In Sec-

tion 2 we briefly describe the EDEN telescopes and our observational methods. Section 3 details our data reduction pipeline before lightcurve detrending and transit search described in Section 4. In Section 5, we provide background on the selected EDEN targets for which we perform a sensitivity analysis in Section 6. Finally, in Section 7 we discuss our planet detection limits in the context of M-dwarf planetary occurrence rates, known systems, and NASA’s *TESS* mission.

2. OBSERVATIONS

We briefly describe the EDEN telescopes, survey target selection, and photometric data collection procedures in order to provide context for our data reduction, transit search, and sensitivity analysis methods. A nuanced discussion of our strategy for selecting and observing targets, and a comparison with other surveys, will be reserved for a future paper (Apai et al. in prep.), and only necessary details are included here.

2.1. Observatories

EDEN observations are currently conducted with eight unique telescopes at seven observatories in North America, Europe, and Asia. The telescopes are the Kuiper 1.55 m (Mount Bigelow, Arizona), Bok 2.3 m (Kitt Peak, Arizona), Vatican Advanced Technology Telescope 1.8 m (VATT; Mount Graham, Arizona), Phillips 0.6 m and Schulman 0.8 m (Mount Lemmon, Arizona), Calar Alto 1.23 m (Calar Alto, Spain), Cassini 1.52 m (Mount Orzale, Italy), and Lulin 1 m (Mount Lulin, Taiwan). Table 1 details the location, design, and CCD imager of each telescope. With the exception of the robotic Schulman and Phillips telescopes, each of them is manually controlled by an observer, who actively monitors weather conditions and instrument performance during the course of a night. While the telescope designs are varied, each of the telescopes has been carefully evaluated for photometric performance before its inclusion in EDEN and, when necessary, changes have been made in the telescope’s operation and setup, which will be detailed in Apai et al. (in prep.). Systematic differences between telescopes therefore have very minor effects on the final lightcurves and transit search. These differences can be compensated for during the data reduction and detrending steps, discussed in Section 3 and 4.

The majority of the EDEN telescopes are not solely dedicated to EDEN, so observations are scheduled at each facility individually in blocks usually from two to ten days per month, depending on availability. Observing science targets at these sites has been ongoing since June 2018 (following a six-month-long EDEN pilot pro-

¹ <http://project-eden.space>

gram), with observations of the targets discussed in this paper occurring between June 2018 and February 2019.

2.2. Target Selection

EDEN’s primary focus is to search for potentially habitable planets within 15 pc (~ 50 lightyears). Correspondingly, for the EDEN Transit Survey, our target selection prioritizes M4 and later-spectral-type host stars, which offer favorable planet-to-star projected areal ratios, making broadly Earth-sized planets detectable in our data. We eliminate known close binary stars that may reduce the stability of putative planets and would complicate the interpretation of the lightcurve. We then prioritize sources that are too faint ($I > 15$ mag) to be efficiently searched by TESS or are outside TESS’s sky coverage. In addition to these high-priority EDEN targets we also include separately targets of particular interest in our source catalog. Such targets may be exoplanet candidate host stars (from radial velocity or transit searches), for which EDEN data can prove valuable for candidate verification. Such follow-up targets (where prior knowledge about a planet’s presence exists) will not be used in future exoplanet occurrence rate studies.

2.3. Science Observations

EDEN targets, including those discussed in this paper, are late-M dwarfs scattered throughout the Northern Hemisphere sky and thus must be observed one at a time. For planets orbiting within or interior to the habitable zone of these stars (e.g., [Kasting et al. 1993](#); [Kopparapu et al. 2014](#)), expected transit durations range from 0.5 to 3 hours at periods of roughly 0.5 to 10 days.

To maximize the probability of observing transits with these parameters and to take advantage of the longitudinal coverage of EDEN telescopes, we designed our observing strategy around two pillars. First, we observe each target for as long as possible on a given night. This typically means that on a clear night we observe a primary target for > 6 hr, and then a secondary target for 2–3 hr when the primary is not observable. This also increases the chance of observing a full transit, which is easier to detrend and detect than fractional transits. Second, whenever possible, we schedule simultaneous observing campaigns in Arizona, Europe, and Taiwan to allow the potential for continuous 24 hour monitoring of one target for multiple days. On such longer, coordinated runs—given good weather at all sites—we can obtain roughly week-long continuous sequences, limited only by our allocated time on these facilities.

These pillars allow us to quickly get good phase coverage of a target for shorter-period planets. Practically, continuous observation has been difficult to fully exploit

because of the rarity of getting good weather on three continents during the entire run. The number of nights dedicated to any target is based on the probability that we would have observed two transits of a planet with an orbital period of less than 10 days. As this probability increases, we deprioritize a given target so that more targets can be adequately sampled. While it is not practically possible to reach 100% detection probability for planets throughout the entire habitable zone (from inner to outer edge, [Kopparapu et al. 2014](#)), we aim to reach high sensitivity for transiting planets that orbit at the inner edge of the habitable zone (i.e., $\sim 50\%$ successful detection of Earth-size transiting planets), which typically translates to some sensitivity ($\gtrsim 10\%$) throughout the habitable zone.

2.3.1. Observational Procedures

Although each of our telescopes has somewhat different capabilities and performance, we adopt the same observational procedures at each telescope to minimize systematic differences.

Filter—For each telescope we use a near-infrared (NIR) (or blue-blocking) filter, such as Harris-I or similar. This filter choice maximizes the collected photons from our targets, which are brightest in the NIR, while blocking unwanted sky background from the Moon and skyglow. Since Spring 2019, the filter has been standardized at all telescopes to an uncoated GG 495² glass long-pass filter (transparent at > 500 nm). Redder filters such as *I* or *z'* have been occasionally used for bright targets if the sky background is very high, for example, during a full moon. The *z'* is otherwise generally avoided because of the low quantum efficiency of most CCD detectors at those wavelengths and the greater presence of telluric absorption bands from water vapor ([Bailer-Jones & Lamm 2003](#); [Blake et al. 2008](#)).

Exposure Time—The exposure time is chosen to balance competing signal-to-noise and cadence considerations. We never allow the peak target flux to go above $\sim 60\%$ the detector’s full well, where the detector begins to exhibit non-linear behavior. In a given period of time, such as a transit duration, the total Poisson-noise-driven signal-to-noise ratio (SNR) follows the relationship

$$SNR_{\text{tot}} \propto \sqrt{\frac{R}{1+R}},$$

where R is the ratio of the exposure time to readout time ([Howell & Tavackolimehr 2019](#)). This relationship

² www.us.schott.com

Table 1. EDEN Telescopes

Telescope	Location	Operation	Mount	CCD Imager	Det. Size	FOV	Px. Scale	Q_e at 700 nm
Phillips 0.6 m	Mount Lemmon, Arizona	Robotic	EQ	SBIG STX (KAF- 16803)	4096×4096	22′×22′	0.35″	40%
Schulman 0.8 m	Mount Lemmon, Arizona	Robotic	EQ	SBIG STX (KAF- 16803)	4096×4096	22′×22′	0.35″	40%
Lulin 1.0 m	Mount Lulin, Taiwan	Classical	EQ	Sophia 2048B CCD	2048×2048	13.08′×13.08′	0.39″	60%
Calar Alto 1.23 m	Calar Alto, Spain	Remote	EQ	DLR- MKIII camera with e2v CCD231- 84-NIMO- BI-DD sensor	4k×4k	21.5′ × 21.5′	0.31″	93%
Cassini 1.52 m	Mount Orzale, Italy	Classical	EQ	Bologna Faint Object Spectro- graph and Camera	1300×1340	13′×12.6′	0.34″	75%
Kuiper 1.55 m	Mount Bigelow, Arizona	Classical	EQ	Mont4K SN3088 (Weiner et al. 2018)	4096×4097	9.7′×9.7′	0.14″	62%
VATT 1.8 m	Mount Graham, Arizona	Classical	Alt-Az	VATT4K STA0500A CCD	4064×4064	12.5′×12.5′	0.188″	80%
Bok 2.3 m	Kitt Peak, Arizona	Classical	EQ	90 Prime Focus Wide- Field Imager (G. Grant Williams 2004)	4×4032× 4096	1.16°×1.16°	0.4″	80%

levels off at $R \sim 3.5$, and we thus aim for an exposure time of $\sim 3.5 \times$ the readout time. For our telescopes with a diameter larger than one meter and targets with magnitude $I \sim 14$, this gives a cadence < 60 s.

Focus—Previous work (e.g., Southworth et al. 2009) has shown that defocusing can result in more precise lightcurves as the point spread function (PSF) is spread across more pixels. We aim for a slight-to-moderate defocus of 2–3″, so that pixel-to-pixel variations are re-

duced, but the PSF maintains a Gaussian shape. Since defocusing also reduces the peak of the PSF, it has the additional benefit of allowing longer exposures.

2.4. Calibration Frames

We follow standard calibration procedures for flat, bias, and dark corrections to reduce systematic effects on our lightcurves. Detailed tests (complete re-reduction and analysis of selected datasets) show that the de-

tails of the basic calibration do not affect the resulting lightcurve precision significantly.

For our calibration procedure, before or after every night of observation, we collect ~ 10 twilight flat-fields with exposure times chosen to maintain a sky flux approximately at 50% the detector’s full well, the same as our desired peak target flux. In some cases of inclement weather during twilight, we may use dome flats, but these are not preferred since they have less uniform illumination. The minimum flat exposure time is always long enough so that the shutter time has $<1\%$ effect on the precision of the flat.

Generally, at least once per observing run, we collect a set of bias and dark frames. The dark current for our exposure times is nearly zero at all telescopes and is usually not subtracted. At some telescopes darks are not collected for this reason. There is no evidence for persistence on any of our detectors.

3. DATA REDUCTION

EDEN data reduction is performed with a custom Python-based automatic pipeline, `edenAP`, which is based on a precursor pipeline for reducing Las Cumbres Observatory Global Telescope (LCOGT) lightcurves (Brown et al. 2013). `edenAP` is designed to accommodate the particularities of the individual telescopes in the EDEN telescope network and reduce the data in a consistent manner. Differences that must be accounted for include number and configuration of chip amplifiers, and pixel scale. `edenAP` is called locally when new raw data arrive, and produces a comparison-star-detrended (Section 3.4) lightcurve for each observation as its final output, which can be further detrended and used for a transit search. The pipeline is highly automated and, in the event of improvements to the algorithm, `edenAP` can be re-run on all previous data with minimal effort. All raw data are stored at the University of Arizona, as well as through a cloud storage provider (Amazon Web Services).

3.1. Science Calibration

The first step in `edenAP` is to calibrate the raw science frames using the calibration frames discussed in Section 2.4. In the event that calibration frames are not available or are of poor quality, this step can be skipped with the rest of the pipeline remaining the same. To create master calibration frames, we collect all bias frames within one month of the observation, and all dark and flat frames within the observation run. Monitoring of flat fields has indicated that these stay mostly constant over the course of a run, with the exception of minor localized dust accumulation and chance occurrences such

as insects getting trapped in the optical path. In cases where many hundreds of calibration frames are available in the above time periods, we narrow the period and only collect calibration frames within two to three days of the observation.

3.2. Astrometry

We then derive the astrometric solution for every science frame by using a local installation of the `astrometry.net` software package (Lang et al. 2010). While this solution provides accurate astrometric calibration for most frames, it can fail in case of partial cloud cover or poor seeing. If no astrometric solution can be found for a particular image, the solution from the preceding image is used, despite these data typically being very poor. The astrometric solution derived is used as a first guess for placing photometric apertures, however, we always refine the centroid using the `photutils`³ `DAOStarFinder` method (Bradley et al. 2019), based on the `DAOFIND` algorithm (Stetson 1987). Position refinement is key to getting sub-pixel centroid precision, especially for our high proper motion target stars.

3.3. Photometry

Aperture photometry is performed using the `photutils` package (Bradley et al. 2019). For every star in the field of view, we measure the intensity in apertures ranging from 5 to 50 pixels in steps of 1 pixel. The aperture size that minimizes the RMS scatter of the target star lightcurve is selected as the best aperture for all sources. The optimal size depends on detector and seeing, but typical size are roughly a few arcseconds. Sky background is calculated as the median of a 60×60 pixel sub-image around the star with other sources clipped. Photometry is saved into a Python pickle file with other important information for each star, such as centroid positions, stellar magnitudes, background, FWHM, airmass, etc., which can later be used for detrending steps and vetting transit-like signals.

3.4. Comparison Star Detrending

The final step in `edenAP` is to detrend the target lightcurve on the basis of comparison star lightcurves. Trends are long or short term photometric variations in the lightcurve that decrease transit detection sensitivity, and can arise from instrumental, atmospheric, and stellar variability. We select the best comparison stars by first filtering out stars that are saturated, are too faint (several magnitudes dimmer than the target) or have too

³ <https://photutils.readthedocs.io/en/stable/>

many failed photometric measurements. Next, we divide the flux normalized target lightcurve by the normalized lightcurves of every comparison star, and rank them based on the average standard deviation in windows of 20 data points. The six with the lowest average deviation (i.e. those with the most similar data trends) are median-combined into a “super comparison” lightcurve, which is then divided from the target lightcurve. For crowded fields with many available comparison stars, it is conceivable that this selection method could weaken or remove transit signals. We believe this is highly unlikely, however, due to the improbability that comparison lightcurves would have the necessary shape to remove a transit, and because the duration of the window is shorter than any expected non-grazing transit. Nevertheless, we account for this in our sensitivity analysis (Section 6.2) by re-selecting comparison stars after injecting transits.

4. TRANSIT SEARCH

In the subsequent steps we identify and remove residual systematic trends (i.e., those not shared fully by comparison stars) and search for lightcurve features that are candidate transit events. Our approach is a modular, automatic, step-by-step process that is robust and easily repeatable, allowing for detailed test runs and process optimization. As detailed in the following subsections, we use a simple median-detrending method and base our vetting methods on instrumental parameters, such as airmass and centroid position, to attempt to explain observed trends and transit-like features. The end result is either a promising candidate, triggering follow-up observations, or sensitivity limits if no convincing candidate is found. A discussion of transit candidate follow-up is reserved for a future paper (Apai et al., in prep.).

4.1. Interactive Data Viewer

We visually inspect every lightcurve on a single EDEN target to ensure that lightcurve anomalies are recognized and managed correctly. We select high-quality data for further analysis without relying on automatic algorithms. To streamline this process, we have implemented an interactive data viewer that displays each lightcurve along with systematic trends, allowing the user to flag large sections of problematic data (e.g., stellar flares, passing clouds) for removal and points of interest (a transit-like feature) for further analysis. Excluding poor-quality data is exceedingly important because strong systematic trends can be fit as transits, and they can throw off the correct period determination if one transit of an otherwise detectable period happened to occur within it. Individual outlier data points are ig-

nored in this step, but are efficiently removed by our automatic filtering in the next step.

4.2. Median Detrending

After visual inspection, lightcurves undergo automated data cleaning and detrending. We fit a long-term trend with a median filter of two hours and 2σ -clip upper outlying data before dividing out the trend. We do not clip below the median because of the risk of clipping deep transits. Median filtering will reduce the depth of all transits slightly, though our use of a two-hour filter window minimizes this effect for transits with durations of less than one hour, which comprises most of our discovery space. An example of median detrending applied to a real EDEN lightcurve with an injected transit of $\sim 1\%$ depth and TRAPPIST-1 b parameters is shown in Figure 1.

While median detrending is a simple method, its effects are predictable and robust. Although the median filtering will not remove short-period, transit-like trends, it will not remove real transits either, if they are deeper than a few tenths of a percent (a danger of more complicated detrending techniques). Other trend-fitting methods with which we have experimented when performing transit injection tests include Savitzky-Golay (Savitzky & Golay 1964), biweight, and multivariate polynomials constructed from external parameters such as airmass, and centroid positions. Savitzky-Golay and biweight filtering have very similar results to median detrending, and while multivariate polynomials can outperform median filters, they are also more likely to accidentally remove a real transit feature. Despite their relative simplicity, median filters are reliable (Hippke et al. 2019).

4.3. Transit Least Squares

To search for transits in our detrended lightcurves, we utilize the package **Transit Least Squares** (TLS, Hippke & Heller 2019). The primary improvement over box least squares (BLS, Kovács et al. 2002) is that rather than fitting a boxcar model to a time series, TLS fits a more realistic, fixed transit shape with limb-darkening included, but the same parameters as BLS otherwise. We optimize the TLS algorithm for our search by setting upper and lower limits on the stellar radius and mass to those for M dwarfs ($0.1 - 0.6R_{\odot}$, $0.08 - 0.5M_{\odot}$) and the maximum period to correspond to the approximate outer edge of the habitable zone (~ 10 days). We rely on our previously described data cleaning and detrending steps to remove bad data, and all lightcurves are weighed equally regardless of photometric precision. For each search we save a median-smoothed periodogram, as well as the phase folded model, transit parameters, false

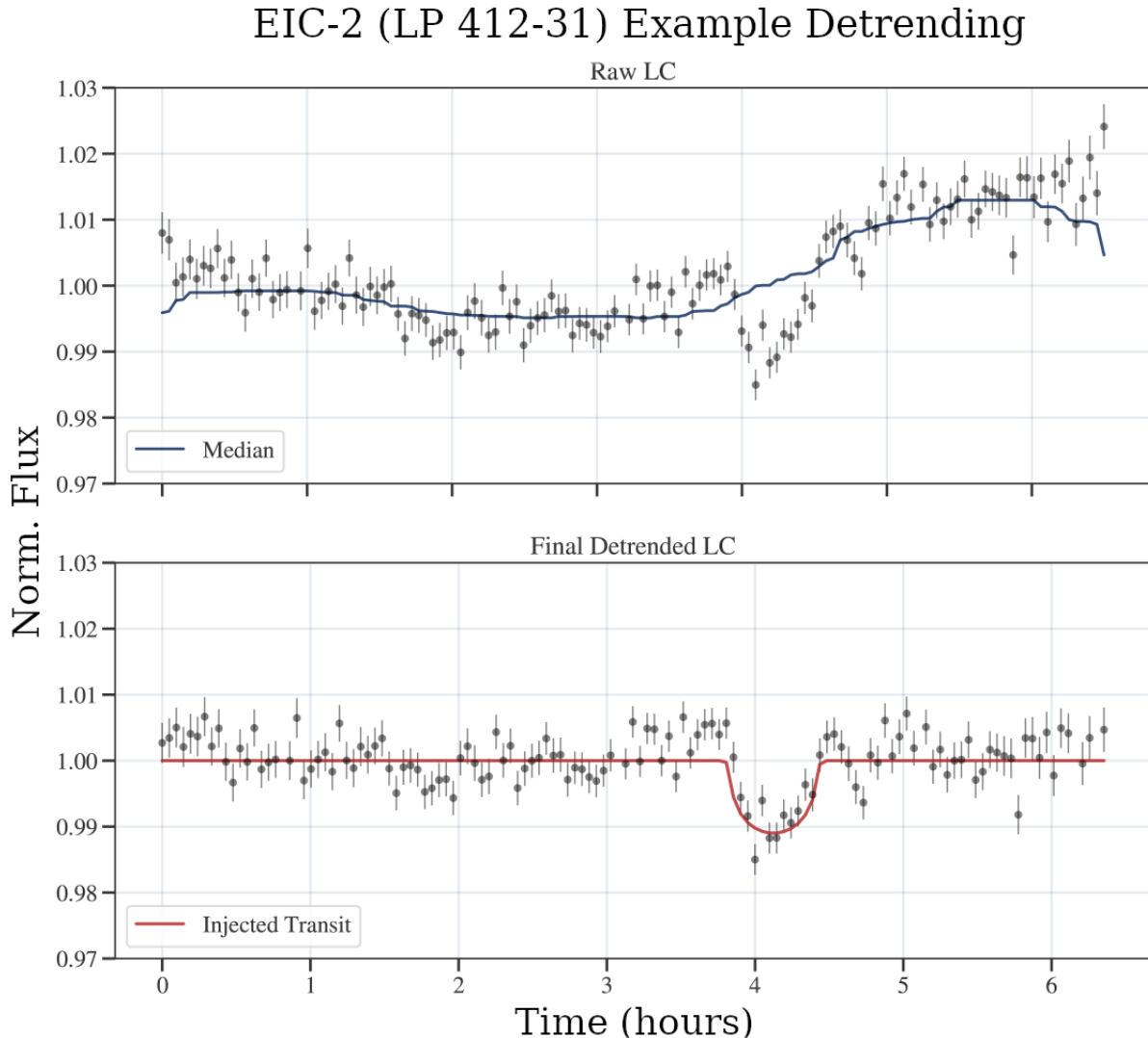


Figure 1. EIC-2 (LP 412-31) Example Detrending. Data was taken with the Cassini telescope on 2018-12-11. The red line at bottom shows the injected transit signal (depth $\sim 1\%$, TRAPPIST-1 b orbit, with limb-darkening from Claret (1998)) compared to the lightcurve after median detrending has been applied. The median shown at top is affected by some points outside the flux range.

alarm probability (FAP), and signal detection efficiency (SDE) for the highest power period.

4.4. Candidate Vetting

Most transit candidates identified by TLS are false positives—and often obvious ones. Currently, vetting is done manually, but it may be automated in the future. The first check of a candidate is inspection of the viability of the TLS output: are the transit parameters physical, does the phase folded lightcurve have obvious flares or systematic trends, what are the SDE and FAP values? If these are viable, the interactive data viewer is used to look at systematic trends during transit times, which usually reveal systematic noise sources that in-

troduced the feature. We pursue follow-up observation to eliminate astrophysical false positives (such as eclipsing binaries) only after identifying a promising transit candidate not explainable by other means. We do not specifically set SDE or FAP values to eliminate transit candidates, and consider even those with poor statistics. However, we do perform an analysis of the SDE and FAP values that indicate a robust detection in Section 6.

5. THE FIRST EDEN TARGETS

EIC-1 (*2MASS J1835379+325954*), EIC-2 (*LP 412-31*), and EIC-3 (*2MUCD 20263*) are all nearby M8/8.5 ultracool dwarfs (Table 2). They are near the hydrogen burning limit and thus may be either high-mass brown

dwarfs or low-mass stars. In this section we will briefly describe their stellar properties and past observations relevant to a search for planets.

5.1. EIC-1

2MASS J1835379+325954, hereafter EIC-1, is an M8.5V dwarf located 5.7 parsecs away (Reid et al. 2003). It was discovered and identified as a nearby dwarf by Lépine et al. (2002) as part of the Digitized Sky Survey. Its brown dwarf status is currently unknown due to differing lines of evidence (Saur et al. 2018; Reiners & Basri 2009; Berdyugina et al. 2017). It is a known radio pulsator with a strong magnetic field and a rapid 2.84 hr rotation period (Berger et al. 2008; Berdyugina et al. 2017; Kuzmychov et al. 2017; Hallinan et al. 2008, 2015). A possible detection of auroral emission has recently been reported for this target (Hallinan et al. 2015).

EIC-1 has been the target of radial velocity (RV) observations by CARMENES (Tal-Or et al. 2018) and Keck NIRSPEC (Tanner et al. 2012), some photometric monitoring by MEarth (Dittmann et al. 2016), a wide-orbiting companion search by *Spitzer* IRAC (Carson et al. 2011), and Subaru adaptive optics (AO) observations (Siegler et al. 2005), as well as numerous spectroscopic studies from UV to radio wavelengths. We are unaware of any companion candidates from these observations, but note that CARMENES identified it as “active RV-loud”, potentially making the detection of habitable planets difficult by RV. EIC-1 was not observed by *K2* and is scheduled to be observed by *TESS* in Sector 26 in June 2020.

5.2. EIC-2

LP 412-31, hereafter EIC-2, is an M8V dwarf located 14.7 parsecs away, identified by Kirkpatrick et al. (1995). It has a rotational period of 0.61 days (Irwin et al. 2011) and is a known flare star with a previously observed giant flare by XMM-Newton (Stelzer et al. 2006).

EIC-2 has been the target of RV observations by the Red-Optical Planet Survey (Barnes et al. 2014) and Keck NIRSPEC (Rodler et al. 2012; Tanner et al. 2012), which have 2σ sensitivity to $M \sin i > 3.0M_{\oplus}$ throughout the habitable zone. It has also had periodic observations by MEarth (Dittmann et al. 2016). It was not monitored by *K2* or *Spitzer* and is not scheduled to be observed by *TESS* until after the primary mission due to its location near the ecliptic.

5.3. EIC-3

2MUCD 20263, hereafter EIC-3, is an M8 dwarf located 15.6 parsecs away, identified by Lépine & Shara (2005). Compared to EIC-1 and EIC-2, it has been the

target of relatively few observations. It has been observed as part of MEarth and the SDSS-III APOGEE Radial Velocity Survey (Deshpande et al. 2013). It was not observed by *K2* or *Spitzer* and is scheduled to be observed by *TESS* in Sector 20 in January 2020.

6. PLANET DETECTION LIMITS FOR EIC-1, EIC-2, AND EIC-3

In this section we report the results of our previously described observations, data reduction and detrending pipelines, and transit search for the first three EDEN targets. Both visual and automatic transit injection and recovery tests are performed, described in Sections 6.2.2 and 6.2.3 respectively. We do not detect any convincing planet candidates for these stars, but place sensitive upper limits on the presence of transiting planets around them.

6.1. Description of Lightcurves

EIC-1, EIC-2, and EIC-3 were observed for 200 to 300 hours each from June 2018 to February 2019, with 40 to 60 individual observations per target (see Table 3). The observations are highly clustered in time, with a few periods of continuous or nearly-continuous observations at different observatories lasting 24 hours or more.

Roughly 60–80% of the cleaned, detrended data are of sufficient quality for a subsequent transit search; the rest is affected by bad weather conditions or technical issues. Durations for the individual high-quality lightcurves range between 2 and 10 hours, depending on target priority, observability, and weather. Some gaps less than 2 hours long exist within longer lightcurves because of passing clouds, temporary technical issues, or manual removal of flares or poor data sections. Cadences vary by a factor of ~ 2 – 3 depending on the telescope (with higher cadence for larger primary mirrors) and detector readout times. The average median unbinned precision for lightcurves on a target is $\sim 0.28\%$. Trends are variable, but most lightcurves have nearly linear or parabolic variations of 1–3% over their duration, possibly attributable to changing airmass or pointing drift. A sample of detrended lightcurves for EIC-2 for each telescope is shown in Figure 2.

Each target shows evidence for stellar activity, which is expected given their spectral type and previous observations described in Section 5. EIC-2 and EIC-3 have occasional flaring activity above 1%. Lightcurve segments with clearly-identifiable flares were removed manually before the transit search. Less than five flares were removed for both targets, representing a negligible loss in time. EIC-1 exhibits regular variability with a 0.5% to 1% amplitude, consistent with the rotational period

Table 2. EDEN Targets

ID	Name	Spec. Type	Dist. (pc)	<i>I</i> Mag	<i>K</i> Mag	R.A. (J2000)	Decl. (J2000)
EIC-1	2MASSI J1835379 +325954	M8.5V	5.7	13.46	9.17	18:35:37.88	+32:59:53.31
EIC-2	LP 412-31	M8V	14.7	14.48	10.64	03:20:59.71	+18:54:22.77
EIC-3	2MUCD 20263	M8	15.6	14.35	10.84	07:14:03.94	+37:02:46.03

of ~ 3 hr (Berger et al. 2008). This variation can mimic transit-like signals, and thus reduces our transit detection sensitivity for the target.

6.2. Sensitivity Analysis

To assess the transit detection capability of our observations, we implement a transit injection and recovery routine. We inject realistic transits into our raw target lightcurves using the analytic solutions of Mandel & Agol (2002) as implemented in `batman` (BASIC TRANSIT MODEL CALCULATION, Kreidberg 2015), re-select comparison stars with the same procedure described in Section 3.4, and attempt to recover the transit signals using our detrending and transit search pipeline. We also perform a limited visual transit recovery test to compare the sensitivity of the pipeline to a manual search by eye.

6.2.1. Manual Transit Search

Before injecting any simulated transits, we perform a TLS search and manual inspection of the lightcurves for each target to attempt to identify real transit candidates. Three team members reviewed every lightcurve individually and marked features of interest (transit candidates), which were then compared and vetted together according to Section 4.4, along with the transit candidates identified by TLS. We do not consider any of the transit candidates to be likely planets worthy of follow-up observation; we instead find them to be consistent with stellar variability and systematics. These steps do not definitively exclude the presence of transiting planets, but the probability of detecting a transiting planet is low, and will be quantified through our sensitivity analysis.

6.2.2. Visual Transit Recovery Tests

As a comparison to the following TLS sensitivity results in Section 6.2.3, we also performed a limited, visual transit injection and recovery test. The purpose was to probe what transits team members could find by eye, without prior knowledge of their existence or location.

One team member injected a TRAPPIST-1 b analog ($1.1 R_{\oplus}$, $\sim 0.7\%$ depth, 1.51 day period, Gillon

et al. 2017) at a random phase into a fraction of the lightcurves of each target (see Section 6.2.3 for other parameters). Three other team members each received independent sets of these lightcurves with injections at random phase. Nearly half of the lightcurve sets did not contain any injections so that the team would not be compelled to identify transit candidates if they believed none were convincing.

True positives are defined as real injections that are correctly identified, false positives are non-injection features wrongly identified as transits, and false negatives are real injections not identified. Collectively, out of 41 observed injected transits in 5 different sets of lightcurves, the team had a 1:1 true to false positive ratio, and a 4:1 false negative to true positive ratio. To determine our average visual sensitivity to TRAPPIST-1 b analogs, we consider how many sets of target lightcurves (containing multiple observed transit injections) had at least one true positive, irrespective of false negatives. Four out of five sets of target lightcurves with injections had one or more true positive, therefore we consider our average visual sensitivity to TRAPPIST-1 b analogs to be $\sim 80\%$. We believe this is limited by conservative transit identification rather than poor data quality. In reality, the false negative ratio is not as high as 4:1 since some of the “observed” transit injections are essentially unidentifiable due to only a small fraction of the transit being observed. While these tests are not a rigorous assessment of our ability to detect transits by eye, they support our argument that Earth-size planets can be correctly identified in our lightcurves without relying on the automated search routine.

6.2.3. Automated Transit Recovery Tests

The purpose of our automatic transit injection and recovery tests is to provide a scalable and objective sensitivity analysis method. For these tests, we simulate transits for planets in a logarithmic grid of period and radius from 0.5 to 10 days and 0.6 to 4 Earth radii, respectively, constituting most of our expected discovery space. The stellar radii of the target stars

Table 3. Log of Observations

ID	Name	Nights Obs.	Hours Obs.	Median Unbinned Precision (%)	% used for TLS
EIC-1	2MASSI J1835379 +325954	57	205.3	0.163	~70
EIC-2	LP 412-31	56	311.7	0.315	~70
EIC-3	2MUCD 20263	43	297.5	0.380	~85

NOTE—Appendix A provides a detailed log of the observations.

Sample Detrended Lightcurves for EIC-2 (LP 412-31)

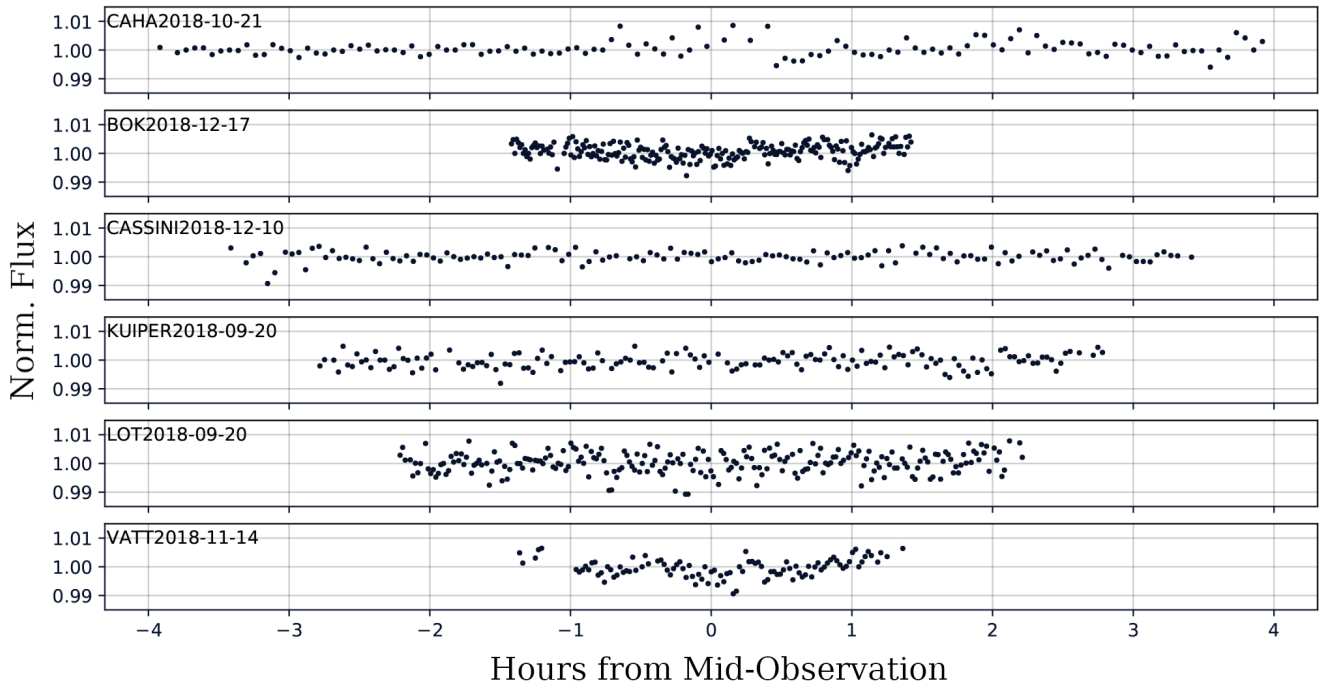


Figure 2. EIC-2 (LP 412-31) Sample Lightcurves. The data are unbinned so that the relative cadence and raw precision of the instruments can be seen. Telescope and date are shown in the top left for each lightcurve.

were determined from available surface gravity measurements (Tsuji & Nakajima 2016; Rajpurohit et al. 2018). Within the grid, orbits are assumed to be circular with random phases and with impact parameters randomly drawn from a uniform distribution between 0.0 and 1.0. While it is technically feasible to detect transits up to an impact parameter of $1 + R_p$, 1.0 is chosen as the upper limit since our detrending and search pipeline is not optimized to search for the very short duration and altered limb-darkening of grazing transits, and will have reduced sensitivity in that parameter space. We empirically find that sensitivity begins to drop significantly

around impact parameters of 0.9, with around half the sensitivity to impact parameters between 0.9 and 1.0 compared to the average sensitivity below 0.9. Furthermore, a limit of $1 + R_p$ creates an artificial dependence on planet radius for transit sensitivity analysis, which distracts from more meaningful sensitivity trends.

The transit injections have quadratic limb darkening laws from Claret (1998) for the I band. While other limb darkening laws (e.g., logarithmic or exponential) may be more realistic (Espinoza & Jordán 2016), the differences for the sensitivity analysis are negligible in the present noise level regime. We further assume that

the limb-darkening laws will be similar in all our NIR and red filters, and thus we use the same law for every injection.

Planets are injected at each grid point until there are 10 potentially detectable planets, i.e., planets with at least one simulated transit within the observing windows. This procedure is adopted to have a sufficient number of detectable planets at longer periods for counting statistics, where many planets may have no observed transits based on their random phase. Combining the grid size (12 by 8) with the requirement of 10 detectable planets means that, for each target, there are a total of 960 potentially recoverable transiting planets in the global sensitivity map.

6.2.4. Positive Identification of Transits

For us to consider a transit detected by TLS to be a true positive result, it must meet one of the following two criteria: (1) the best period is less than 0.5 hours different from the true period of the injected planet, or (2) at least one identified transit midpoint time is within 20 minutes of a real injected transit midpoint (i.e., a transit candidate was correctly identified, but the period is incorrect). All candidates which meet condition one, naturally meet condition two.

We make an additional distinction between true positives recovered by TLS and “successful recoveries”, which we count in our sensitivity analysis. Successful recoveries are a subset of true positives that also pass a detection significance criterion. We make this distinction because it is possible in a real search to detect a shallow transit only to dismiss it due to low signal. We do not want to consider these cases as successful in our analysis. Therefore, we limit successful recoveries in this analysis to detections that exceed a minimum signal detection efficiency (SDE) (Hippke & Heller 2019), corresponding to a detection in a real search that would likely pass vetting and trigger follow-up observations. The SDE is the significance of a period relative to the average significance of all other periods.

We determine the minimum SDE for each target individually based on the global SDE distribution of false positives resulting from our injection recoveries. We set the minimum SDE required for a successful detection as the SDE that is greater than 95% of false positives (i.e., only 5% of false positives have a higher SDE). For our three targets, the minimum robust SDE value ranges for EIC-1, 2 and 3, are roughly 6, 7, and 11.

The true and false positive distributions are shown for EIC-1, EIC-2, and EIC-3 in Figure 3. The differences result from the unique structure of each target’s set of lightcurves, which produce higher and lower significance

false positives. One noticeable feature of these plots (especially for EIC-3) is that the false positive distribution does not continually increase for lower SDE values, but is instead centered at a specific SDE. This potentially counter-intuitive distribution is caused by both the structure of each target’s set of lightcurves, as well as the range and step size of the injection grid. Each target has a dominant false positive signal that is returned when there is no transit injection. Our grid range includes two rows of sub-Earth size planets that are extremely shallow in depth, and each injection in these rows will return nearly the same false positive SDE as if there was no injection. This leads to a build-up of a high fraction of false positives around the no injection SDE value, which corresponds roughly to the maximum of the false positive distribution. The higher fraction of true positives at lower SDE values is due to the fact that there is a certain range of injection depths that will only be a marginally higher power than the no injection false positive and thus will have a low SDE, but they will still be detected successfully at high rates.

It is important to note that the SDE cutoff is not used to determine the significance of transit candidates in the real transit search and is only used in finding the significance of injection recoveries after concluding by other means (Section 6.2.1) that the data contains no real transits. Therefore, it likely provides a conservative sensitivity estimate. Finally, the SDE cutoff cannot be expected to fully capture the probability that a true positive candidate would be followed-up and confirmed, but rather is a best attempt at conservatively estimating the likelihood given subjective human involvement in deciding what is and what is not a convincing candidate. While it would be more desirable to build a completely automatic vetting algorithm, for our observations the algorithm would need to be prohibitively intelligent and complex, and could result in more missed planets.

6.2.5. Pipeline Sensitivity

We illustrate our transit detection sensitivity for EIC-1, EIC-2, and EIC-3 in Figures 4, 5, and 6, respectively. The top plots show the efficiency of our pipeline to detect transiting planets, while the bottom plots represent total detection probability for all planets, both transiting and non-transiting, based on our transit detection sensitivity and the geometric transit probability for planets as a function of semi-major axis ($P_{tr} = \frac{R_*}{a}$). To calculate the overall sensitivity within a specific range of periods and radii, we simply average the detection sensitivity in that range. Mean sensitivities for select ranges are shown in Table 4.

Table 4. EDEN Sensitivity

ID	Transit Sensitivity (%)			Total Detectability (%)		
	0.5 to 2 days	2 to 5 days	5+ days	0.5 to 2 days	2 to 5 days	5+ days
EIC-1	60 ± 10	35 ± 5	12 ± 1	4.0 ± 0.5	1.1 ± 0.25	0.18 ± 0.05
EIC-2	40 ± 10	22 ± 5	10 ± 1	2.5 ± 0.5	0.6 ± 0.25	0.17 ± 0.05
EIC-3	80 ± 10	40 ± 5	8 ± 1	5.3 ± 0.5	1.1 ± 0.25	0.13 ± 0.05

NOTE—Reported transit sensitivity and total detectability values are averages for planets between one and two Earth radii. Listed errors are the standard error of the mean.

7. DISCUSSION

7.1. EDEN Sensitivity

The sensitivity maps for EIC-1, EIC-2, and EIC-3 show that we have the potential to successfully detect transiting Earth-sized planets in the habitable zones of nearby, ultracool dwarfs. Furthermore, they show that in a few cases we can detect sub-Earth-sized planets on closer orbits provided two or more transits occur during high-quality observations. To compare these results with *TESS*, the estimated photometric precisions for EIC-1, EIC-2, and EIC-3 are 0.136, 0.299, and 0.343 % respectively in *one hour* periods of observation (*TESS* Mag. 13.28, 14.35, and 14.52) (Stassun et al. 2018). These are very similar to the median achieved precisions of unbinned EDEN lightcurves typically at a *one minute* cadence (0.163, 0.315, and 0.380 % respectively). Thus, with long-term targeted observations it is possible we could achieve better sensitivities than *TESS* for single targets, in cases where the benefit of our increased photometric precision can outweigh the benefit of *TESS*'s continuous 28 day coverage.

7.2. Sensitivity Analysis and Detection Biases

The primary goal of our sensitivity analysis is setting planetary limits around the target stars that will be useful for future observations. These limits can potentially improve the efficiency of similar transit surveys, and in the case of any future radial velocity (RV) companion candidates, help to constrain the inclination. The secondary goal is to help to identify strengths, weaknesses, and biases of our observations and routines. Using this information we can improve our future observations, data reduction, detrending, and search methods. That being stated, we believe our methods are nearly optimized, and only minor improvements can still be expected, which would not significantly change our sensitivity results.

The sensitivity maps in Figures 4, 5 and 6 show two distinct gradients of decreasing sensitivity. As one would

expect, these gradients are for smaller planets ($< 1R_{\oplus}$, i.e., lower transit signal-to-noise), and longer periods (> 3 days, i.e. fewer observed transits). Both regions of low sensitivity have more true positives than are considered successful, since many detections will have low significance that may not be followed-up. It is possible that some of these true positives would be followed-up, therefore it is likely that the map is somewhat conservative. Furthermore, our manual injection and recovery by eye test estimated that our sensitivity to TRAPPIST-1 b analogs is $\sim 80\%$, while the average automated sensitivity is $\sim 30\%$. This provides additional evidence that the automated sensitivity is conservative, especially for longer period planets where one transit can be successfully detected by eye. As a final point, on the right side of the bottom plot of Figures 4, 5 and 6, where geometric probability is considered, the gradient for longer period planets becomes steeper, reflecting the decreasing transit probability at greater distance from the host star.

One noticeable aspect of our sensitivity maps is higher noise than similar plots from space-based missions. The noise is due to four primary factors, including the limited grid size, random transit times, the relatively low number of planets injected, as well as the sporadic and discontinuous schedule of EDEN observations. Most single blocks with relatively high or low sensitivity are simply due to the random sample times. Unlike observations from *Kepler*, it is possible that by misfortune a short-period planet never transits during an observation. Some columns may also have lower or higher sensitivity compared to their surroundings depending on whether or not the period is close to a harmonic of the period of observations, and therefore are more or less sensitive to phase.

7.3. Inner Planets and Outer Planets

Our detection limits for inner, shorter period planets can place significant constraints on the probability of outer, longer period planets, where observational

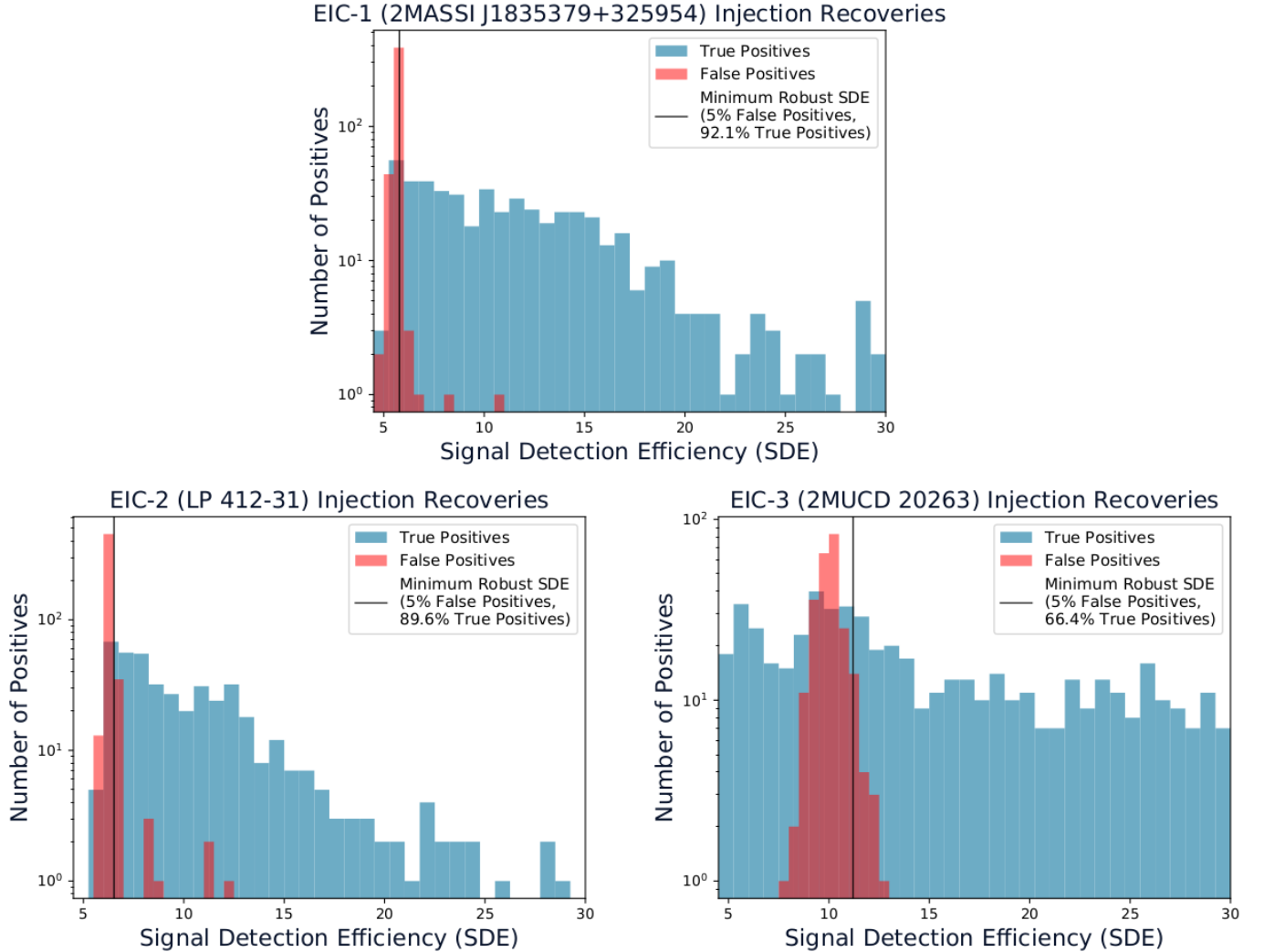


Figure 3. Signal Detection Efficiency (SDE) Distribution for EICs. SDE is calculated as the signal to noise of the highest power in the recovery periodogram (Hippke & Heller 2019). The number of false positives does not continue increasing for lower SDE values because of the characteristic false positive unique to each set of lightcurves. Further discussion can be found in Section 6.2.4.

coverage is lacking, in light of the occurrence rates of small planets around M-dwarfs (Mulders et al. 2015a). The strongest example of this is the TRAPPIST-1 system. TRAPPIST-1b and c were detected by ground based observations that motivated space-based follow-up, which discovered longer-period planets. For our targets, the approximate probability to detect transiting planets analogous to TRAPPIST-1b and c with *one or more transits* is $\sim 50\%$. The lack of close-in transiting planets in the extensive datasets on our targets decreases the probability that there are transiting planets at longer periods, and suggests continued observation to increase sensitivity for them is not be pragmatic, given the much larger volume of data needed.

7.4. Constraints on Planet Formation Theory

The sample of planets around very cool stars is still small, since late M-dwarfs are too faint for wide-field transit surveys. In addition, higher stellar activity can further complicate the analyses of their lightcurves (e.g., Perger et al. 2017). EDEN has unique capabilities to target these stars and any planet our survey may detect will serve as a valuable addition to this small sample. The examples of TRAPPIST-1 (Gillon et al. 2017) and GJ 3512b (Morales et al. 2019) showed how individual discoveries can challenge our current understanding of planet formation and inform tests of competing formation theories. To assess such discoveries in terms of the actual underlying population of exoplanets, it is crucial to be aware of and able to quantify the relevant selection

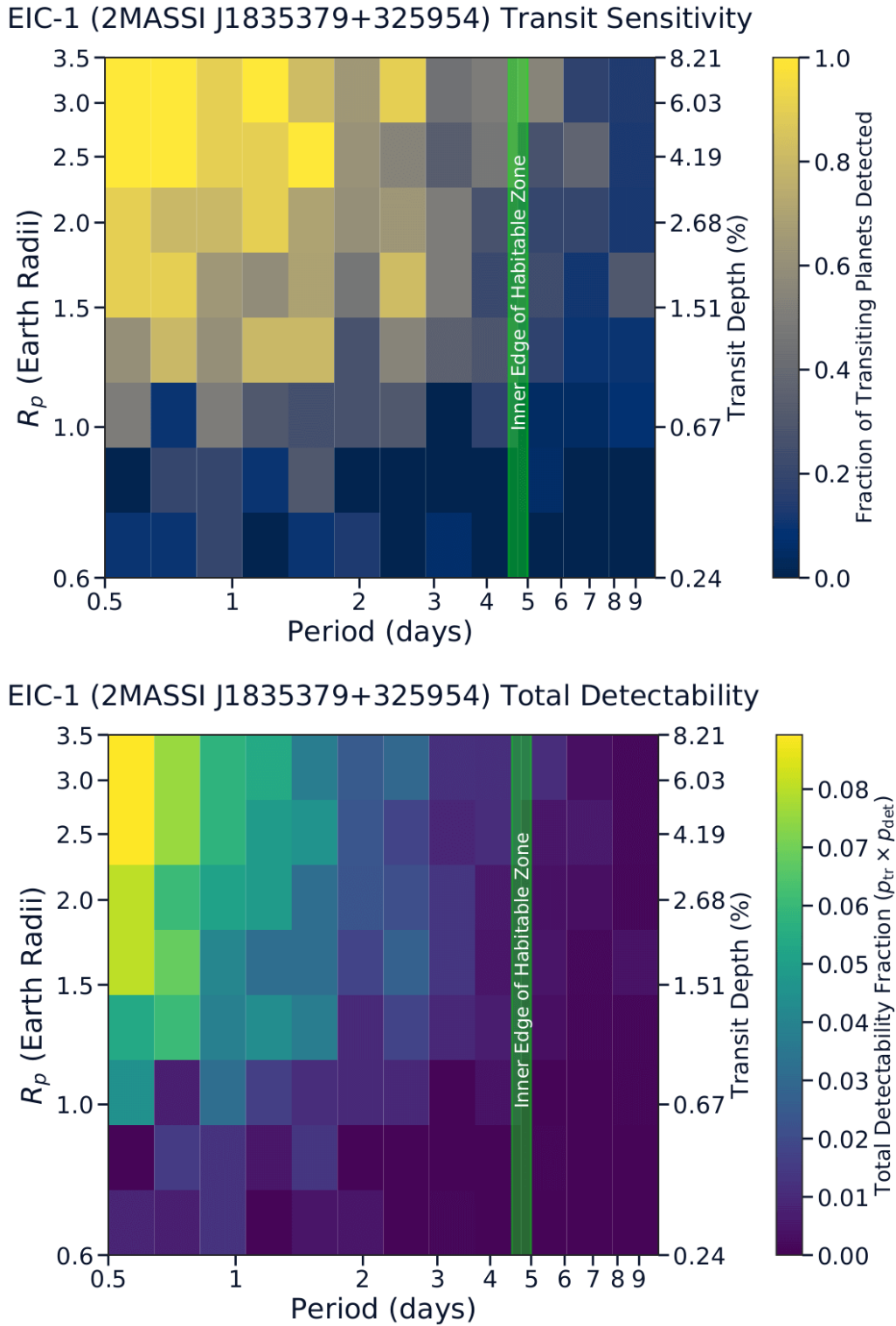


Figure 4. EIC-1 (2MASSI J1835379+325954) sensitivity maps. Top: Pipeline sensitivity to transiting planets. Each grid block represents the fraction of transiting planets recovered out of all injected planets (both recoverable and non-recoverable) for a period and radius centered within the block. Bottom: Total detectability considering the geometric transit probability ($p_{tr} \times p_{det}$).

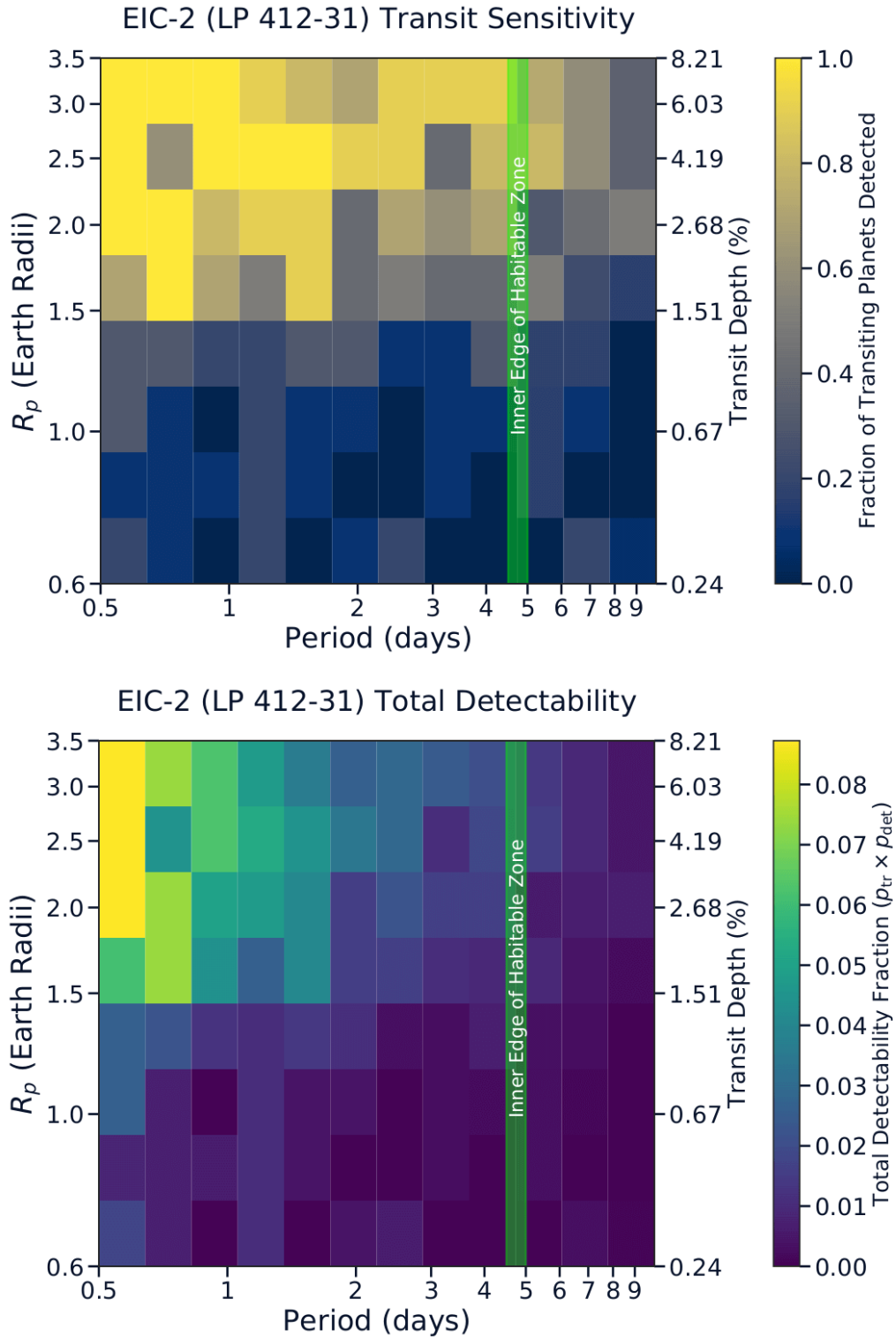


Figure 5. EIC-2 (LP 412-31) sensitivity maps. Top: Pipeline sensitivity to transiting planets. Each grid block represents the fraction of transiting planets recovered out of all injected planets (both recoverable and non-recoverable) for a period and radius centered within the block. Bottom: Total detectability considering the geometric transit probability ($p_{tr} \times p_{det}$).

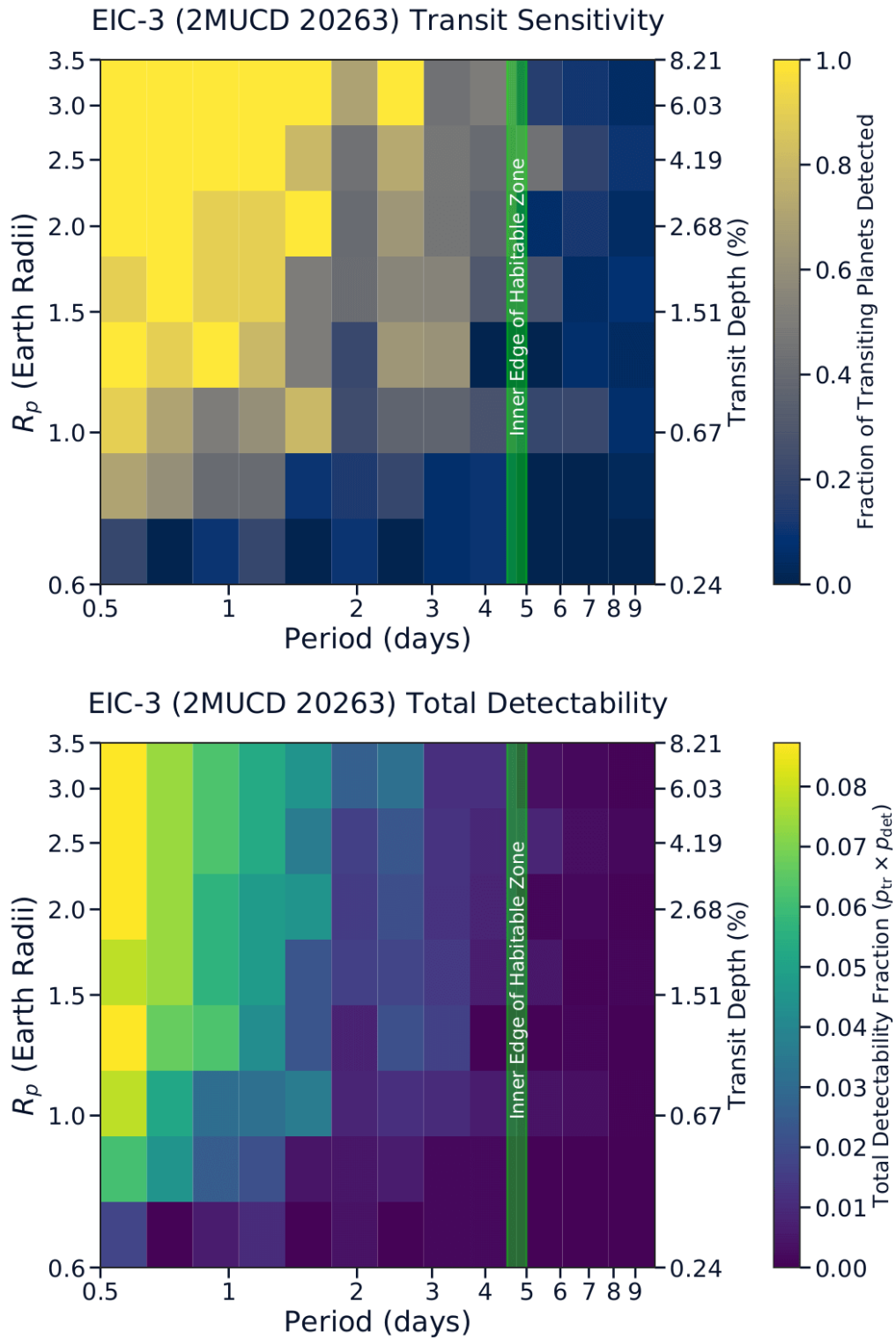


Figure 6. EIC-3 (2MUCD 20263) sensitivity maps. Top: Pipeline sensitivity to transiting planets. Each grid block represents the fraction of transiting planets recovered out of all injected planets (both recoverable and non-recoverable) for a period and radius centered within the block. Bottom: Total detectability considering the geometric transit probability ($p_{tr} \times p_{det}$).

biases. With a well-defined target selection function, an automated detection pipeline, and the thorough sensitivity analysis presented here, we are prepared to accurately model the EDEN selection biases. Correcting for these biases enables detailed occurrence rate measurements and builds the foundation to study the demographics of late M-dwarf planetary systems.

The inferred bias can also be applied to synthetic planets from a theoretical formation model. The resulting *observable* synthetic population enables statistical comparisons between theory and observations (e.g., [Mordasini et al. 2009](#)). Detailed forward models of well-characterized exoplanet surveys can directly test planet formation models and even optimize free parameters ([Mulders et al. 2018, 2019](#)). Such dedicated M-dwarf population syntheses are powerful tools to constrain planet formation in a parameter space different from that around solar-type stars. The predictive power of exoplanet surveys depends on the survey’s sensitivity and the number of targets observed: as the number of targets observed by EDEN increases, the emerging planet statistics will increase in significance. Currently, we are surveying targets at an increasing rate.

8. CONCLUSIONS

We present the first lightcurves and sensitivity analysis from the EDEN transiting exoplanet survey. The key results of our studies are as follows:

1) EDEN’s 0.6–2.3 m diameter telescopes provide very high-quality (median 0.28% precision) red-visual (500–900 nm) lightcurves for late-M-dwarf stars in the solar neighborhood.

2) We present data on three nearby late-M dwarfs, obtained in the context of a multi-continental transit search campaign. Our observations include 57, 56, and 43 nights of data on the three targets (EIC-1, EIC-2, EIC-3), respectively.

3) We reviewed the EDEN data reduction and photometry pipeline and our de-trending and transit search procedure. Our procedure has been tested, optimized, and validated through transit injection-and-recovery tests.

4) Our lightcurves reach the sensitivity to detect transits of Earth-sized planets. In the total of 156 observations on the three targets, no convincing candidate transit events have been identified.

5) We describe our transit injection-and-recovery-based approach to assess sensitivity to planetary transits as a function of planet radius and orbital period. We provide a detailed assessment of the sensitivity to transits around our three targets. We show these estimates

are conservative compared to manual transit searches by eye.

6) Our data can confidently exclude the presence of Earth-sized transiting planets with orbital periods shorter than 1 day around each of the targets. Earth-sized planets with 1–2 day periods would have been detected in our data in two transits with $\sim 60\%$ probability.

7) EDEN reaches a sensitivity to Earth-sized planets around faint red dwarf stars ($I \approx 15$ mag), which are challenging targets even for NASA’s *TESS* mission. Thus, EDEN data on such systems can provide complementary information to *TESS* lightcurves.

8) Our study demonstrates the potential of the EDEN survey to robustly probe the presence of transiting, Earth-sized planets within and inside of the habitable zones of nearby late red dwarfs and, in case of non-detection, to set stringent upper limits on the presence of such planets.

ACKNOWLEDGMENTS

The results reported herein benefited from collaborations and/or information exchange within NASA’s Nexus for Exoplanet System Science (NExSS) research coordination network sponsored by NASA’s Science Mission Directorate. This study used results from the RECONS project (recons.org). T. Henning acknowledges support from the European Research Council under the Horizon 2020 Framework Program via the ERC Advanced Grant Origins 83 24 28. B.V. Rackham acknowledges support from the Heising-Simons Foundation.

This research made use of Photutils, an Astropy package for detection and photometry of astronomical sources ([Bradley et al. 2019](#)).

The principal investigators of EDEN are D. Apai, P. Gabor, T. Henning, and W-P. Chen. Initial target selection was performed by A. Mousseau, A. Bixel, and D. Apai. Telescope allocation is organized by D. Apai, L. Mancini, W-P. Chen, C.C. Ngeow, and P. Gabor. Observations have been performed by H. Baehr, A. Bhandare, A. Bixel, R. Boyle (pilot studies as VATT’s Telescope Scientist), S. Brown, J. Dietrich, A. Gibbs, M. Häberle, W. Ip, M. Keppler, L. Mancini, V. Marian, K. Molaverdikhani, A. Mousseau, J. Perez Chavez, B. Rackham, P. Sarkis, M. Schleckler, Q.J. Socia, A. Tsai and others. Software has been developed by A. Bixel, N. Espinoza, A. Gibbs, J. Perez Chavez, and B. Rackham. The EDEN automatic pipeline (**edenAP**) was developed by N. Espinoza (precursor pipeline), B. Rackham (bulk development), A. Bixel, J. Perez Chavez (calibration steps), and A. Gibbs. Data organization and collec-

tion, and the interactive data viewer were developed by A. Bixel. Detrending, transit search, sensitivity analysis steps have been implemented and developed by A. Gibbs.

This research has made use of the Cassini 1.52 m telescope, which is operated by INAF-OAS “Osservatorio di Astrofisica e Scienza dello Spazio” of Bologna in Loiano (Italy).

We thank the mountain operations staff at the University of Arizona, Mount Lemmon Sky Center, Lulin Observatory, Calar Alto Observatory, Loiano Telescopes, Mount Graham International Observatory, Vatican Ad-

vanced Technology Telescope, and Kitt Peak National Observatory.

Facilities: Mount Lemmon Sky Center, Lulin Observatory, Calar Alto Observatory, Loiano 152cm Cassini Telescope, Kuiper 61-inch Telescope, Vatican Advanced Technology Telescope (VATT), Bok 2.3m Telescope

Software: Numpy (van der Walt et al. 2011), Pandas (McKinney 2010), Scipy (Virtanen et al. 2019), Astropy (Price-Whelan et al. 2018), Photutils (Bradley et al. 2019), astronomy.net (Lang et al. 2010), TLS (Hippke & Heller 2019), batman (Kreidberg 2015), edenAP

APPENDIX

A. OBSERVATION LOG

In case of future research or discoveries where EDEN data may be useful, we list all periods of observations for EIC-1, EIC-2, and EIC-3 in Tables 5, 6, and 7.

REFERENCES

- Bailer-Jones, C. A. L., & Lamm, M. 2003, MNRAS, 339, 477, doi: [10.1046/j.1365-8711.2003.06189.x](https://doi.org/10.1046/j.1365-8711.2003.06189.x)
- Barnes, J. R., Jenkins, J. S., Jones, H. R. A., et al. 2014, Monthly Notices of the Royal Astronomical Society, 439, 3094, doi: [10.1093/mnras/stu172](https://doi.org/10.1093/mnras/stu172)
- Berdugina, S. V., Harrington, D. M., Kuzmychov, O., et al. 2017, ApJ, 847, 61, doi: [10.3847/1538-4357/aa866b](https://doi.org/10.3847/1538-4357/aa866b)
- Berger, E., Basri, G., Gizis, J. E., et al. 2008, ApJ, 676, 1307, doi: [10.1086/529131](https://doi.org/10.1086/529131)
- Blake, C. H., Bloom, J. S., Latham, D. W., et al. 2008, Publications of the Astronomical Society of the Pacific, 120, 860, doi: [10.1086/590506](https://doi.org/10.1086/590506)
- Bradley, L., Sipocz, B., Robitaille, T., et al. 2019, astropy/photutils: v0.6, doi: [10.5281/zenodo.2533376](https://doi.org/10.5281/zenodo.2533376)
- Brown, T. M., Baliber, N., Bianco, F. B., et al. 2013, PASP, 125, 1031, doi: [10.1086/673168](https://doi.org/10.1086/673168)
- Carson, J. C., Marengo, M., Patten, B. M., et al. 2011, ApJ, 743, 141, doi: [10.1088/0004-637X/743/2/141](https://doi.org/10.1088/0004-637X/743/2/141)
- Claret, A. 1998, VizieR Online Data Catalog, 333
- de Wit, J., Wakeford, H. R., Gillon, M., et al. 2016, Nature, 537, 69, doi: [10.1038/nature18641](https://doi.org/10.1038/nature18641)
- de Wit, J., Wakeford, H. R., Lewis, N. K., et al. 2018, Nature Astronomy, 2, 214, doi: [10.1038/s41550-017-0374-z](https://doi.org/10.1038/s41550-017-0374-z)
- Delrez, L., Gillon, M., Queloz, D., et al. 2018, in Society of Photo-Optical Instrumentation Engineers (SPIE) Conference Series, Vol. 10700, Proc. SPIE, 107001I, doi: [10.1117/12.2312475](https://doi.org/10.1117/12.2312475)
- Deshpande, R., Blake, C. H., Bender, C. F., et al. 2013, AJ, 146, 156, doi: [10.1088/0004-6256/146/6/156](https://doi.org/10.1088/0004-6256/146/6/156)
- Dittmann, J. A., Irwin, J. M., Charbonneau, D., & Newton, E. R. 2016, ApJ, 818, 153, doi: [10.3847/0004-637X/818/2/153](https://doi.org/10.3847/0004-637X/818/2/153)
- Dressing, C. D., & Charbonneau, D. 2015, ApJ, 807, 45, doi: [10.1088/0004-637X/807/1/45](https://doi.org/10.1088/0004-637X/807/1/45)
- Espinoza, N., & Jordán, A. 2016, MNRAS, 457, 3573, doi: [10.1093/mnras/stw224](https://doi.org/10.1093/mnras/stw224)
- G. Grant Williams, Ed Olszewski, M. P. L. J. H. B. 2004, 90prime: a prime focus imager for the Steward Observatory 90-in. telescope, doi: [10.1117/12.552189](https://doi.org/10.1117/12.552189)
- Gillon, M., Triaud, A. H., Demory, B. O., et al. 2017, Nature, 542, 456, doi: [10.1038/nature21360](https://doi.org/10.1038/nature21360)
- Greene, T. P., Line, M. R., Montero, C., et al. 2016, ApJ, 817, 17, doi: [10.3847/0004-637X/817/1/17](https://doi.org/10.3847/0004-637X/817/1/17)
- Hallinan, G., Antonova, A., Doyle, J. G., et al. 2008, ApJ, 684, 644, doi: [10.1086/590360](https://doi.org/10.1086/590360)
- Hallinan, G., Littlefair, S. P., Cotter, G., et al. 2015, Nature, 523, 568, doi: [10.1038/nature14619](https://doi.org/10.1038/nature14619)
- Hardegree-Ullman, K. K., Cushing, M. C., Muirhead, P. S., & Christiansen, J. L. 2019, arXiv e-prints, arXiv:1905.05900. <https://arxiv.org/abs/1905.05900>
- Henry, T. J., Jao, W.-C., Winters, J. G., et al. 2018, AJ, 155, 265, doi: [10.3847/1538-3881/aac262](https://doi.org/10.3847/1538-3881/aac262)
- Hippke, M., David, T. J., Mulders, G. D., & Heller, R. 2019, AJ, 158, 143, doi: [10.3847/1538-3881/ab3984](https://doi.org/10.3847/1538-3881/ab3984)

- Hippke, M., & Heller, R. 2019, *A&A*, 623, A39, doi: [10.1051/0004-6361/201834672](https://doi.org/10.1051/0004-6361/201834672)
- Howell, S. B., & Tavackolimehr, A. 2019, *Handbook of CCD Astronomy*
- Irwin, J., Berta, Z. K., Burke, C. J., et al. 2011, *ApJ*, 727, 56, doi: [10.1088/0004-637X/727/1/56](https://doi.org/10.1088/0004-637X/727/1/56)
- Jehin, E., Gillon, M., Queloz, D., et al. 2011, *The Messenger*, 145, 2
- Kasting, J. F., Whitmire, D. P., & Reynolds, R. T. 1993, *Icarus*, 101, 108, doi: [10.1006/icar.1993.1010](https://doi.org/10.1006/icar.1993.1010)
- Kirkpatrick, J. D., Henry, T. J., & Simons, D. A. 1995, *AJ*, 109, 797, doi: [10.1086/117323](https://doi.org/10.1086/117323)
- Kopparapu, R. K., Ramirez, R. M., SchottelKotte, J., et al. 2014, *The Astrophysical Journal*, 787, L29, doi: [10.1088/2041-8205/787/2/129](https://doi.org/10.1088/2041-8205/787/2/129)
- Kovács, G., Zucker, S., & Mazeh, T. 2002, *A&A*, 391, 369, doi: [10.1051/0004-6361:20020802](https://doi.org/10.1051/0004-6361:20020802)
- Kreidberg, L. 2015, *PASP*, 127, 1161, doi: [10.1086/683602](https://doi.org/10.1086/683602)
- Kuzmychov, O., Berdyugina, S. V., & Harrington, D. M. 2017, *ApJ*, 847, 60, doi: [10.3847/1538-4357/aa705a](https://doi.org/10.3847/1538-4357/aa705a)
- Lang, D., Hogg, D. W., Mierle, K., Blanton, M., & Roweis, S. 2010, *AJ*, 139, 1782, doi: [10.1088/0004-6256/139/5/1782](https://doi.org/10.1088/0004-6256/139/5/1782)
- Lépine, S., & Shara, M. M. 2005, *AJ*, 129, 1483, doi: [10.1086/427854](https://doi.org/10.1086/427854)
- Lépine, S., Shara, M. M., & Rich, R. M. 2002, *AJ*, 124, 1190, doi: [10.1086/341783](https://doi.org/10.1086/341783)
- Lustig-Yaeger, J., Meadows, V. S., & Lincowski, A. P. 2019, *AJ*, 158, 27, doi: [10.3847/1538-3881/ab21e0](https://doi.org/10.3847/1538-3881/ab21e0)
- Mandel, K., & Agol, E. 2002, *ApJL*, 580, L171, doi: [10.1086/345520](https://doi.org/10.1086/345520)
- McKinney, W. 2010, in *Proceedings of the 9th Python in Science Conference*, ed. S. van der Walt & J. Millman, 51 – 56
- Morales, J. C., Mustill, A. J., Ribas, I., et al. 2019, *Science*, 365, 1441
- Mordasini, C., Alibert, Y., Benz, W., & Naef, D. 2009, *Astronomy and Astrophysics*, 501, 1161, doi: [10.1051/0004-6361/200810697](https://doi.org/10.1051/0004-6361/200810697)
- Morley, C. V., Kreidberg, L., Rustamkulov, Z., Robinson, T., & Fortney, J. J. 2017, *ApJ*, 850, 121, doi: [10.3847/1538-4357/aa927b](https://doi.org/10.3847/1538-4357/aa927b)
- Mulders, G. D., Mordasini, C., Pascucci, I., et al. 2019, arXiv e-prints. <https://arxiv.org/abs/1905.08804>
- Mulders, G. D., Pascucci, I., & Apai, D. 2015a, *ApJ*, 798, 112, doi: [10.1088/0004-637X/798/2/112](https://doi.org/10.1088/0004-637X/798/2/112)
- . 2015b, *ApJ*, 814, 130, doi: [10.1088/0004-637X/814/2/130](https://doi.org/10.1088/0004-637X/814/2/130)
- Mulders, G. D., Pascucci, I., Apai, D., & Ciesla, F. J. 2018, *AJ*, 156, 24, doi: [10.3847/1538-3881/aac5ea](https://doi.org/10.3847/1538-3881/aac5ea)
- Nutzman, P., & Charbonneau, D. 2008, *PASP*, 120, 317, doi: [10.1086/533420](https://doi.org/10.1086/533420)
- Perger, M., García-Piquer, A., Ribas, I., et al. 2017, *A&A*, 598, A26, doi: [10.1051/0004-6361/201628985](https://doi.org/10.1051/0004-6361/201628985)
- Price-Whelan, A. M., Sipőcz, B. M., Günther, H. M., et al. 2018, *AJ*, 156, 123, doi: [10.3847/1538-3881/aabc4f](https://doi.org/10.3847/1538-3881/aabc4f)
- Rajpurohit, A., Allard, F., Teixeira, G. D. C., et al. 2018, *A&A*, 610, A19, doi: [10.1051/0004-6361/201731507](https://doi.org/10.1051/0004-6361/201731507)
- Reid, I. N., Cruz, K. L., Laurie, S. P., et al. 2003, *AJ*, 125, 354, doi: [10.1086/344946](https://doi.org/10.1086/344946)
- Reiners, A., & Basri, G. 2009, *ApJ*, 705, 1416, doi: [10.1088/0004-637X/705/2/1416](https://doi.org/10.1088/0004-637X/705/2/1416)
- Ricker, G. R., Winn, J. N., Vanderspek, R., et al. 2015, *Journal of Astronomical Telescopes, Instruments, and Systems*, 1, 014003, doi: [10.1117/1.JATIS.1.1.014003](https://doi.org/10.1117/1.JATIS.1.1.014003)
- Rodler, F., Deshpande, R., Zapatero Osorio, M. R., et al. 2012, *A&A*, 538, A141, doi: [10.1051/0004-6361/201117577](https://doi.org/10.1051/0004-6361/201117577)
- Saur, J., Fischer, C., Wennmacher, A., et al. 2018, *The Astrophysical Journal*, 859, 74, doi: [10.3847/1538-4357/aabb55](https://doi.org/10.3847/1538-4357/aabb55)
- Savitzky, A., & Golay, M. J. E. 1964, *Analytical Chemistry*, 36, 1627, doi: [10.1021/ac60214a047](https://doi.org/10.1021/ac60214a047)
- Siegler, N., Close, L. M., Cruz, K. L., Martin, E. L., & Reid, I. N. 2005, *The Astrophysical Journal*, 621, 1023, doi: [10.1086/427743](https://doi.org/10.1086/427743)
- Southworth, J., Hinse, T. C., Jorgensen, U. G., et al. 2009, *Monthly Notices of the Royal Astronomical Society*, 396, 1023, doi: [10.1111/j.1365-2966.2009.14767.x](https://doi.org/10.1111/j.1365-2966.2009.14767.x)
- Stassun, K. G., Oelkers, R. J., Pepper, J., et al. 2018, *AJ*, 156, 102, doi: [10.3847/1538-3881/aad050](https://doi.org/10.3847/1538-3881/aad050)
- Stelzer, B., Schmitt, J. H. M. M., Micela, G., & Liefke, C. 2006, *A&A*, 460, L35, doi: [10.1051/0004-6361:20066488](https://doi.org/10.1051/0004-6361:20066488)
- Stetson, P. B. 1987, *PASP*, 99, 191, doi: [10.1086/131977](https://doi.org/10.1086/131977)
- Tal-Or, L., Zechmeister, M., Reiners, A., et al. 2018, *A&A*, 614, A122, doi: [10.1051/0004-6361/201732362](https://doi.org/10.1051/0004-6361/201732362)
- Tanner, A., White, R., Bailey, J., et al. 2012, *ApJS*, 203, 10, doi: [10.1088/0067-0049/203/1/10](https://doi.org/10.1088/0067-0049/203/1/10)
- Tinetti, G., Drossart, P., Eccleston, P., et al. 2018, *Experimental Astronomy*, 46, 135, doi: [10.1007/s10686-018-9598-x](https://doi.org/10.1007/s10686-018-9598-x)
- Tsuji, T., & Nakajima, T. 2016, *Publications of the Astronomical Society of Japan*, 68, doi: [10.1093/pasj/psv119](https://doi.org/10.1093/pasj/psv119)
- van der Walt, S., Colbert, S. C., & Varoquaux, G. 2011, *Computing in Science Engineering*, 13, 22, doi: [10.1109/MCSE.2011.37](https://doi.org/10.1109/MCSE.2011.37)
- Virtanen, P., Gommers, R., Oliphant, T. E., et al. 2019, arXiv e-prints, arXiv:1907.10121. <https://arxiv.org/abs/1907.10121>

Wakeford, H. R., Lewis, N. K., Fowler, J., et al. 2019, AJ, 157, 11, doi: [10.3847/1538-3881/aaf04d](https://doi.org/10.3847/1538-3881/aaf04d)

Weiner, B. J., Sand, D., Gabor, P., et al. 2018, in Society of Photo-Optical Instrumentation Engineers (SPIE) Conference Series, Vol. 10704, Proc. SPIE, 107042H, doi: [10.1117/12.2314265](https://doi.org/10.1117/12.2314265)

Zhang, Z., Zhou, Y., Rackham, B. V., & Apai, D. 2018, AJ, 156, 178, doi: [10.3847/1538-3881/aade4f](https://doi.org/10.3847/1538-3881/aade4f)

Table 5. EIC-1 (2MASS J1835379+325954) List of Observations

Telescope	Local Date	BJD Start (−245700)	BJD End (−245700)	Hours
CAHA	2018-06-26	1296.354	1296.681	7.8
CASSINI	2018-06-29	1299.354	1299.612	6.2
CASSINI	2018-06-30	1300.342	1300.607	6.4
CAHA	2018-06-30	1300.356	1300.433	1.9
CAHA	2018-07-01	1301.357	1301.409	1.2
CAHA	2018-07-02	1302.349	1302.407	1.4
CASSINI	2018-07-02	1302.353	1302.379	0.6
CAHA	2018-07-03	1303.354	1303.379	0.6
CAHA	2018-07-04	1304.367	1304.652	6.8
KUIPER	2018-07-18	1318.743	1318.959	5.2
CASSINI	2018-07-19	1319.328	1319.615	6.9
CAHA	2018-07-19	1319.346	1319.564	5.2
KUIPER	2018-07-19	1319.868	1319.982	2.7
CASSINI	2018-07-20	1320.328	1320.599	6.5
CAHA	2018-07-20	1320.348	1320.658	7.5
CASSINI	2018-07-21	1321.33	1321.562	5.6
CAHA	2018-07-22	1322.351	1322.675	7.8
CASSINI	2018-07-23	1323.332	1323.615	6.8
CAHA	2018-07-23	1323.347	1323.454	2.6
CAHA	2018-07-24	1324.346	1324.671	7.8
CASSINI	2018-07-25	1325.5	1325.62	2.9
CAHA	2018-07-25	1325.507	1325.671	3.9
CAHA	2018-07-26	1326.508	1326.671	3.9
LOT	2018-07-29	1329.147	1329.211	1.5
KUIPER	2018-09-03	1365.658	1365.812	3.7
KUIPER	2018-09-04	1366.687	1366.773	2.1
KUIPER	2018-09-05	1367.711	1367.802	2.2
KUIPER	2018-09-06	1368.624	1368.808	4.4
KUIPER	2018-09-07	1369.6	1369.804	4.9
CAHA	2018-09-16	1378.308	1378.493	4.5
CAHA	2018-09-17	1379.299	1379.303	0.1
BOK	2018-09-17	1379.643	1379.753	2.6
LOT	2018-09-18	1379.995	1380.147	3.6
LOT	2018-09-19	1381.022	1381.144	2.9
LOT	2018-09-20	1382.006	1382.143	3.3
CAHA	2018-09-20	1382.297	1382.472	4.2
KUIPER	2018-09-20	1382.605	1382.777	4.1
CAHA	2018-09-21	1383.288	1383.479	4.6
CAHA	2018-09-22	1384.287	1384.486	4.8
CAHA	2018-09-23	1385.304	1385.482	4.3
CAHA	2018-09-24	1386.294	1386.463	4.0
CAHA	2018-09-25	1387.299	1387.423	3.0
SCHULMAN	2018-09-25	1387.605	1387.714	2.6
CAHA	2018-09-28	1390.321	1390.46	3.3
SCHULMAN	2018-09-28	1390.59	1390.729	3.3
CAHA	2018-09-30	1392.278	1392.417	3.3
CAHA	2018-10-17	1409.282	1409.405	3.0
LOT	2018-10-19	1411.061	1411.086	0.6
CAHA	2018-10-19	1411.341	1411.414	1.8
LOT	2018-10-20	1411.964	1412.037	1.8
CAHA	2018-10-22	1414.284	1414.364	1.9
CAHA	2018-10-24	1416.265	1416.366	2.4
CAHA	2018-10-25	1417.253	1417.37	2.8
KUIPER	2018-10-31	1423.597	1423.644	1.1
KUIPER	2018-11-03	1426.555	1426.645	2.2
KUIPER	2018-11-04	1427.55	1427.642	2.2

Table 6. EIC-2 (LP 412-31) List of Observations

Telescope	Local Date	BJD Start (−245700)	BJD End (−245700)	Hours
KUIPER	2018-09-04	1366.798	1367.012	5.1
KUIPER	2018-09-05	1367.817	1368.024	5.0
KUIPER	2018-09-07	1369.812	1370.013	4.8
LOT	2018-09-17	1379.16	1379.372	5.1
CAHA	2018-09-17	1379.48	1379.722	5.8
BOK	2018-09-17	1379.776	1379.874	2.3
LOT	2018-09-18	1380.156	1380.342	4.4
CAHA	2018-09-18	1380.54	1380.719	4.3
LOT	2018-09-19	1381.151	1381.338	4.5
LOT	2018-09-20	1382.15	1382.339	4.5
KUIPER	2018-09-20	1382.787	1383.028	5.8
CAHA	2018-09-21	1383.505	1383.714	5.0
CAHA	2018-09-22	1384.511	1384.716	4.9
CAHA	2018-09-23	1385.502	1385.714	5.1
CAHA	2018-09-24	1386.482	1386.616	3.2
CAHA	2018-09-27	1389.545	1389.712	4.0
CAHA	2018-09-28	1390.484	1390.718	5.6
CAHA	2018-09-30	1392.433	1392.714	6.7
LOT	2018-10-16	1408.199	1408.223	0.6
CAHA	2018-10-17	1409.415	1409.636	5.3
CAHA	2018-10-18	1410.632	1410.651	0.5
LOT	2018-10-19	1411.096	1411.381	6.8
CAHA	2018-10-19	1411.433	1411.505	1.7
LOT	2018-10-20	1412.142	1412.391	6.0
CAHA	2018-10-21	1413.392	1413.723	7.9
CAHA	2018-10-22	1414.378	1414.58	4.9
CAHA	2018-10-23	1415.392	1415.396	0.1
CAHA	2018-10-24	1416.377	1416.734	8.6
CAHA	2018-10-25	1417.38	1417.571	4.6
KUIPER	2018-10-31	1423.662	1424.016	8.5
KUIPER	2018-11-01	1424.66	1425.032	8.9
KUIPER	2018-11-02	1425.687	1425.994	7.4
KUIPER	2018-11-03	1426.658	1427.037	9.1
KUIPER	2018-11-04	1427.683	1428.045	8.7
KUIPER	2018-11-09	1432.627	1432.961	8.0
KUIPER	2018-11-10	1433.64	1434.041	9.6
KUIPER	2018-11-11	1434.605	1435.018	9.9
VATT	2018-11-11	1434.632	1435.013	9.1
VATT	2018-11-12	1435.665	1436.011	8.3
VATT	2018-11-13	1436.664	1437.006	8.2
VATT	2018-11-14	1437.84	1438.002	3.9
VATT	2018-11-15	1438.656	1438.997	8.2
VATT	2018-11-16	1439.767	1440.005	5.7
VATT	2018-11-17	1440.709	1441.006	7.1
VATT	2018-11-18	1441.665	1442	8.0
VATT	2018-11-19	1442.654	1442.997	8.2
CASSINI	2018-11-28	1451.28	1451.499	5.3
CASSINI	2018-11-29	1452.338	1452.46	2.9
CASSINI	2018-12-04	1457.263	1457.537	6.6
KUIPER	2018-12-09	1462.559	1462.892	8.0
CASSINI	2018-12-10	1463.248	1463.539	7.0
CASSINI	2018-12-11	1464.274	1464.545	6.5
BOK	2018-12-17	1470.692	1470.811	2.9
CAHA	2018-12-20	1473.355	1473.46	2.5

Table 7. EIC-3 (2MUCD 20263) List of Observations

Telescope	Local Date	BJD Start (−245700)	BJD End (−245700)	Hours
KUIPER	2018-12-09	1462.903	1463.049	3.5
VATT	2018-12-18	1471.69	1471.944	6.1
VATT	2018-12-19	1472.689	1473.051	8.7
VATT	2018-12-20	1473.696	1473.955	6.2
VATT	2018-12-28	1481.742	1482.059	7.6
VATT	2018-12-29	1482.796	1483.064	6.4
VATT	2018-12-30	1483.774	1484.064	7.0
KUIPER	2019-01-02	1486.675	1487.041	8.8
KUIPER	2019-01-03	1487.762	1488.039	6.6
VATT	2019-01-08	1492.596	1493.044	10.8
CAHA	2019-01-09	1493.326	1493.735	9.8
CAHA	2019-01-10	1494.307	1494.726	10.1
VATT	2019-01-10	1494.806	1494.985	4.3
VATT	2019-01-11	1495.608	1496.034	10.2
CAHA	2019-01-14	1498.27	1498.726	10.9
CAHA	2019-01-15	1499.289	1499.717	10.3
CAHA	2019-01-16	1500.281	1500.469	4.5
LOT	2019-01-17	1500.962	1501.322	8.7
LOT	2019-01-18	1502.043	1502.075	0.8
VATT	2019-01-19	1503.589	1504.015	10.2
VATT	2019-01-20	1504.586	1504.8	5.1
VATT	2019-01-22	1506.657	1507.006	8.4
VATT	2019-01-23	1507.588	1508.002	9.9
BOK	2019-01-24	1508.605	1509.01	9.7
BOK	2019-01-25	1509.582	1509.982	9.6
VATT	2019-01-26	1510.591	1510.987	9.5
VATT	2019-01-27	1511.582	1511.99	9.8
LOT	2019-01-28	1511.959	1512.34	9.1
VATT	2019-01-28	1512.61	1512.743	3.2
LOT	2019-01-29	1512.952	1513.336	9.2
LOT	2019-01-30	1513.968	1514.332	8.7
VATT	2019-01-30	1514.679	1514.703	0.6
LOT	2019-01-31	1514.973	1515.324	8.4
VATT	2019-01-31	1515.663	1515.796	3.2
LOT	2019-02-07	1521.973	1522.3	7.8
LOT	2019-02-08	1523.045	1523.237	4.6
LOT	2019-02-09	1524.031	1524.234	4.9
LOT	2019-02-10	1524.997	1525.192	4.7
LOT	2019-02-11	1526.023	1526.236	5.1
LOT	2019-02-12	1526.967	1527.235	6.4
LOT	2019-02-13	1528.016	1528.17	3.7
LOT	2019-02-14	1528.994	1529.175	4.3